Simple thermodynamic model for the hydrogen phase diagram

Ioan B. Magdău,* Miriam Marqués, Balint Borgulya, and Graeme J. Ackland†
CSEC, SUPA, School of Physics and Astronomy, The University of Edinburgh, Edinburgh EH9 3JZ, United Kingdom
(Received 12 October 2016; revised manuscript received 10 February 2017; published 13 March 2017)

We describe a classical thermodynamic model that reproduces the main features of the solid hydrogen phase diagram. In particular, we show how the general structure types, which are found by electronic structure calculations and the quantum nature of the protons, can also be understood from a classical viewpoint. The model provides a picture not only of crystal structure, but also for the anomalous melting curve and insights into isotope effects, liquid metallisation, and infrared activity. The existence of a classical picture for this most quantum of condensed matter systems provides a surprising extension of the correspondence principle of quantum mechanics, in particular the equivalent effects of classical and quantum uncertainty.

DOI: 10.1103/PhysRevB.95.094107

Solid hydrogen provides one of the greatest examples of complexity emerging from a simple system. An equal mix of protons and electrons is perhaps the most fundamental system in condensed matter. Yet the subtle interplay between thermodynamics and quantum mechanics produces a phase diagram that has defied simple understanding. The situation has recently been further complicated by the discovery of a new phase IV [1–3], reports of further phases V and VI [4–6], and a melting point maximum and minimum [7–14]. Current theoretical work concentrates on finding candidate low-energy structures, characterized by symmetry, solving the electronic structure alongside quantum protons across a range of temperature and pressure. These computationally expensive numerical calculations typically offer little insight into the underlying principles determining the phase stability. Here, instead of striving for quantitative accuracy, we take the opposite approach, asking what is the simplest atomic-level model that reproduces the qualitative phase diagram. Our model is derived from studying energy-minimizing structures [15–21] and trajectories of extensive molecular dynamics simulations performed by us and others [22–25]. We identify three recurrent motifs from which we build a big picture understanding of the thermodynamics of the phase diagram, including metallization and isotope effects.

Currently, theoretical predictions of high-pressure phases are based on density functional calculations (DFT) using the PBE functional. Despite the deficiencies of this method [26,27], improved methods, which include treatment of proton dynamics and electron correlation, lead to quantitative rather than qualitative changes to the calculated phase diagram [26,28–32].

The overall picture emerging from a combination of simulation, spectroscopy, and crystallography is as follows. At low pressure phase I comprises quantum rotor molecules in a close-packed structure. At very low temperature and increased pressure phase II appears. Phase II has x-ray diffraction very similar to phase I, and is assumed to have statically ordered molecular orientations which minimize quadrupole interactions [16,33]. At higher pressure phase III is reported as a layered structure with weakly bonded molecules [17,21,34,35]. Phase IV, stable at higher temperatures, can be viewed as alternating layers of phase-III-like weak molecules and phase-I-like strongly bonded, rotating molecules. Phases named IV′ and V, similar to IV, and a premetallic phase VI have also been reported [4–6]. The lowest known energy candidate for phase II is $P2_1/c$ [16] and for phase III $P6_122$ [21] and $C2/c$-24 [16] below and above 200 GPa, respectively. The liquid, and phases I and IV, are calculated to have rotating molecules, leading to time-averaged symmetry higher than any static atomic arrangement. [9,22,23]. The favored candidates for the metallic phase VI [36] are $Cmca$ and $I4/amd$ [15,37]

The melting curve has a strong positive slope at low pressures, but reaches a maximum at around 900 K and 120 GPa, and then drops. The Clapeyron slope flattens off once the solid transforms to the denser phase IV [9–12,38]. The importance of quantum protons is highly debated [7,39,40]. In phase I the characteristic roton bands indicate that angular momentum, J is a good quantum number, and must combine with the nuclear para or ortho spin state to give an antisymmetric molecular wave function. The zero-point energy (ZPE), phonon free energy, and associated pressure can be approximated in two ways, either via lattice dynamics and the quasiharmonic approximation (LDQHA) [41,42], and anharmonic corrections [43] or via path integral molecular dynamics (PIMD) [44]. LDQHA assumes delocalized, harmonic phonons; PIMD assumes distinguishable atoms: neither approach describes freely rotating molecules.

In our model, free energy for each phase depends on its structure and its constituent objects. The three objects in our model (named S, R, and A) allow both quantum and classical interpretation. S is a spherical molecule, which corresponds to a $J = 0$ quantum rotor ground state, or a time-averaged classical free rotor. R is rodlike, corresponding to the standard classical picture of two atoms connected by a covalent bond, or the $J = 1$ quantum rotor state. Finally, A represents simple spherical atoms: these have unpaired electrons which can explain electrical conductance within our model. For accounting purposes, we consider pairs of type A atoms, and dedimensionalized units.

Only free energy differences determine the phase diagram, so we can measure all energies, volumes, and entropies relative to an appropriate implicit reference, which is phase independent, but without loss of generality may be pressure and temperature dependent.

*i.b.magdau@sms.ed.ac.uk
†gjackland@ed.ac.uk

TABLE I. Parameters for objects and structures. All volumes correspond to molecules (i.e., two atoms) and are described further in the SM. All values are strongly constrained by their well-defined physical meaning: that the parameters all fall within reasonable bounds or can be neglected entirely is a key result of the model.

type i		S	R		A
energy U_i		−2	−2		0
entropy S_i		0.7	0.0		0.0
volume V_i		3.6	2.7		0.8×2
structure j	I/VI	II	III	IV/V	liquid
packing c_j	0.74	0.71	0.74	0.79	0.71
config. entropy S_j	0.0	0.0	0.0	0.0	0.75
bonding U_j	0.0	−0.13	0.0	0.0	0.8

We set the covalent bond in both S and R objects to have energies $U_S = U_R = -2$. Atoms are unbound, so U_A is zero. The S objects have a random orientation, which can be regarded as a classical entropy S_S. These values define the reduced (i.e., dimensionless) energy and entropy units for the model. Finally, we assign volumes to each object. For the S molecule, the volume V_S represents the sphere swept out by the rotator, V_R an ellipsoidal diatomic molecule, and V_A a spherical atom, so clearly $V_S > V_R > V_A$. The actual values used are given in Table I. In these reduced units, V_S corresponds to a sphere of radius 0.95, V_R to a prolate ellipsoidal rod with the same major axis and $b/a = 0.9$, and V_A is a sphere of radius 0.575.

The model is formulated in terms of volumes, so to present the results on a pressure-temperature phase diagram we require an equation of state. We use

$$x(P) = \frac{(2P+1)}{(2P+0.15)},$$

which describes a monotonic volume reduction by a factor of about 7 across the pressure range of interest.

The model's phases are as follows.

(i) Phase I has hexagonal close packing (hcp) of S objects. hcp is the most efficient packing of spheres, with a packing fraction of $c_1 = 0.74$.

$$G_1 = U_S + xPV_S/c_1 - xTS_S.$$

(ii) Phase II, the broken symmetry phase, is a structure in which molecules (R objects) point in directions to minimize the quadrupole-quadrupole interaction energy (U_2). Packing is less efficient than phase I, but the overall density is higher because R molecules have no rotation (i.e., $V_R/c_2 < V_S/c_1$).

$$G_2 = U_2 + U_R + xPV_R/c_2.$$

(iii) Phase III is a more efficient packing of rods (R) than phase II, obtained at the cost of no longer minimizing the quadrupole interactions.

$$G_3 = U_R + xPV_R/c_3 - xTS_R.$$

(iv) Phase IV is a mixed molecular-atomic layered structure [1] with molecular B layers and atomic G layers respectively. Our MD showed such structures with space group $P6/mmm$ as a time average: this comes from the B-layer molecules having spherical symmetry and the time-averaged G layer having sixfold symmetry.

We model the B layers as composed of S objects, and the G layers as A objects. This SA_2 compound is equivalent to the MgB_2 structure, which is one of the most efficient packings of binary hard spheres. Phase IV incorporates all mixed phases IV, IV′, and V [4]. The subtle differences between these phases are not significant to this model, and are described later.

$$G_4 = G_5 = (U_S + U_A)/2 + xP(V_S + V_A)/2c_4 - xT(S_S + S_A)/2.$$

(v) We treat the putative metallic phase VI [36] as a close-packed atomic solid with type A objects. In reality metallic hydrogen may have a more open structure, but this is not yet known.

$$G_6 = U_A + xPV_A/c_1 - xTS_A.$$

(vi) Liquid is a Boltzmann-weighted average of S, R, and A objects (labeled i), with additional configurational entropy $S_{\rm liq}$ and energy $U_{\rm liq}$.

$$G_{\rm liq} = F_{\rm liq} + PV_{\rm liq}$$

with

$$F_{\rm liq} = U_{\rm liq} - TS_{\rm liq} + \left(\sum_i (U_i - TS_i)e^{-G_i/T}\right) \Big/ \mathcal{Z}$$

$$V_{\rm liq} = \frac{x}{C_{\rm liq}\mathcal{Z}}\left(\sum_i V_i \exp(-G_i/T)\right),$$

where i indicates sums over S, R, and A.

$$G_i = U_i + xPV_i - TS_i; \quad \mathcal{Z} = \sum_i \exp(-G_i/T).$$

Terms set to zero in Table I are ignored.

For the structural contributions to free energy, we assume that the only significant deviation from intermolecular bonding between different phases at the same (P, T) conditions comes from quadrupole alignment in phase II, and that the liquid has higher configurational entropy and reduced cohesive energy. We ignore energy and entropy contributions that are similar for all structures: these give a structure-independent contribution to the free energy, which does not affect the relative free energies, which determine the phases diagram.

The final parameter describes zero point vibration. LDQHA and PIMD calculations have shown that ZPE is the dominant contribution from nuclear quantum effects, and the effect on the phase diagram is, to a first approximation, a shift of all phase boundaries to lower temperatures [46]. We understand this as a loose equivalence of quantum and thermal oscillations, and account for it by shifting the $T = 0$ axis up by 0.45. This shift is the only isotope-dependent effect in the model, it distinguishes hydrogen from deuterium, for which it is smaller. The I-II phase boundary in deuterium is then at lower temperatures than for hydrogen, and cuts the $T = 0$ axis at lower pressure, as observed.

Remarkably, the phase diagram produced (Fig. 1) for any sensible choice of parameters has stability regions for the six

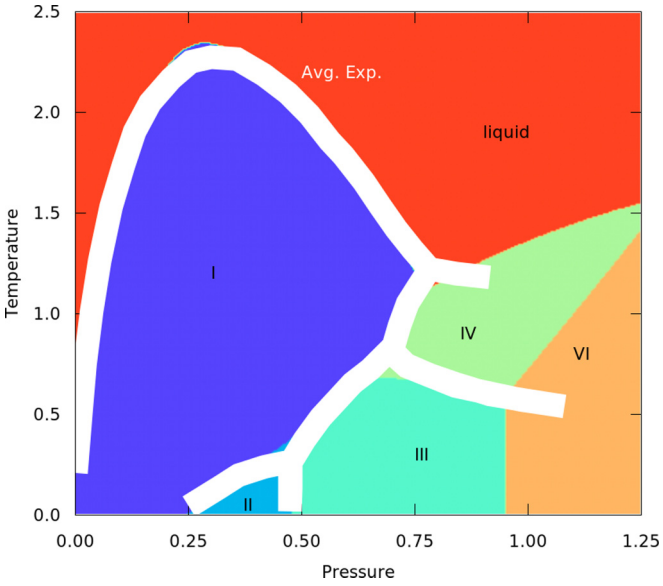

FIG. 1. Phase diagram. Colors depict the phase with lowest Gibbs free energy. Gray lines show the current experimental situation, with approximate uncertainty (see Supplemental Material [45]). Phase IV′ and V are considered as continuous with phase IV. Temperature and pressure are given here in the reduced units of the model, for comparison to experimental GPa and K units, pressure should be scaled by 240 and temperature by 370.

phases in the correct regions of PT space and a melting curve with a maximum.

This gives some insights into the nature of the various phases. The melting temperature maximum means that the liquid has a higher compressibility than the solid. In our model this is because the large S objects in the liquid increasingly convert to smaller R and A objects with pressure. The competing phase I has only large S objects, so becomes less favored at pressure, despite its close packing. Phase IV is assumed denser than the liquid, so its melting point increases with pressure.

The model suggests a novel interpretation of the liquid insulator/metal transition [47,48]. Assuming that molecules (S, R) have localized electrons and atoms have delocalized electrons, conduction occurs once there are sufficient complete paths via neighboring A objects for electron hopping to percolate: this can occur either at high temperature, where all objects are equally likely, or at high pressure where the fraction of smaller A objects is increased.

Phase IV has a free energy advantage over the purely atomic phase thanks to its molecule bonding, and over the pure molecular phase I because of its efficient packing of molecules and atoms. It is stabilized against phase III by the entropy of the rotating S molecules.

The phase diagram shows a positive Clapeyron slope between the atomic (metallic) phase VI and the semiconducting phase IV. There is no thermodynamic reason why a material cannot become metallic on cooling, but it is very unusual. Here, it occurs because of the extra rotor entropy S_S, compared with the zero value of S_A.

The model does not include a zero-temperature quantum liquid phase at high T. This is mainly because we choose not to make the ZPE offset pressure dependent. It is possible to choose parameters for which the melting point goes to zero at high pressure.

Perhaps the most serious simplification entailed by the model compared with our *ab initio* MD [49] comes in the treatment of the so-called graphenelike G layers of phase IV. The structure of phase IV seems well described by *ab initio* molecular dynamics, but although a new phase V was reported recently, our extensive *ab initio* molecular dynamics calculations in this pressure/temperature regime primarily show changes in the dynamics but not in the time-averaged structure. Consequently, phases IV and V are treated the same in our model, as mixed atomic-molecular structures. In MD simulations [22,23,49,50] the G-layer atoms are observed to pair up into short-lived, weakly bound molecules (Fig. 2). We introduced new analysis methods to monitor bond breaking and reconstruction in DFT-MD calculations. This showed that the MgB_2 structure is reasonable as a long time average, but there are subtle changes in symmetry with pressure.

The MD implies that the G layer can be described by decoration of a hexagonal lattice, and the subtle experimental differences between Phases IV, IV′, and V are also consistent with this. Figure 3 gives a schematic view of three possible decorations. In MgB_2, the atoms would be located on the vertices of the lattice (labeled G^a), and molecular dynamics at high pressure shows this structure on average. However, at lower pressures the atoms pair up to form weakly bonded molecules, the weakness evidenced by low-frequency vibrons. The structure has a four-layer BG′BG″ repeat: in the G″ arrangement the molecules form trimers [51] with six atoms inside one in three of the cells of the honeycomb network. In MD, the trimer rotates as a unit. In the G′ arrangement, the molecules are located on the boundaries between cells.

In static relaxation, the B-layer molecules cannot have hexagonal symmetry, and this symmetry breaking induces further symmetry breaking in the G layer. Structure searches have revealed a panoply of such phases [15,18,19]

MD shows continuous transitions between G-layer decorations (Fig. 2). At the onset of phase IV, we find a four-layer stacking with alternating BG′BG″ layers. The yellow-centered atoms and gray rhombus in Fig. 4 show the elegance of this arrangement: notice how the G" trimer is located above the cell in G′, which has no molecules on its boundaries. As pressure increases, all G layers adopt the G′ arrangement at the long time scale, whereas at the short time scales, trimers rebond faster and faster: this is our description for phase V. At still higher pressures the atomic G^a layers are observed.

Phase III has previously been reported as a layered structure, but the logic here requires it to be efficiently packed. This is counter to current understanding, and we have carried out further DFT calculations of the two most likely candidates. Whereas previous work has focused on atoms, in Fig. 5 we show that the ELF isosurfaces of the H_2 molecules are close to ellipsoidal, and the molecule centres themselves are arranged very close to hcp.

This is represented by ordered R objects in our model. The fundamental description of phase III is close packing of molecules. Candidate structures for phase III are based on layers such as that shown in Fig. 6, with molecules

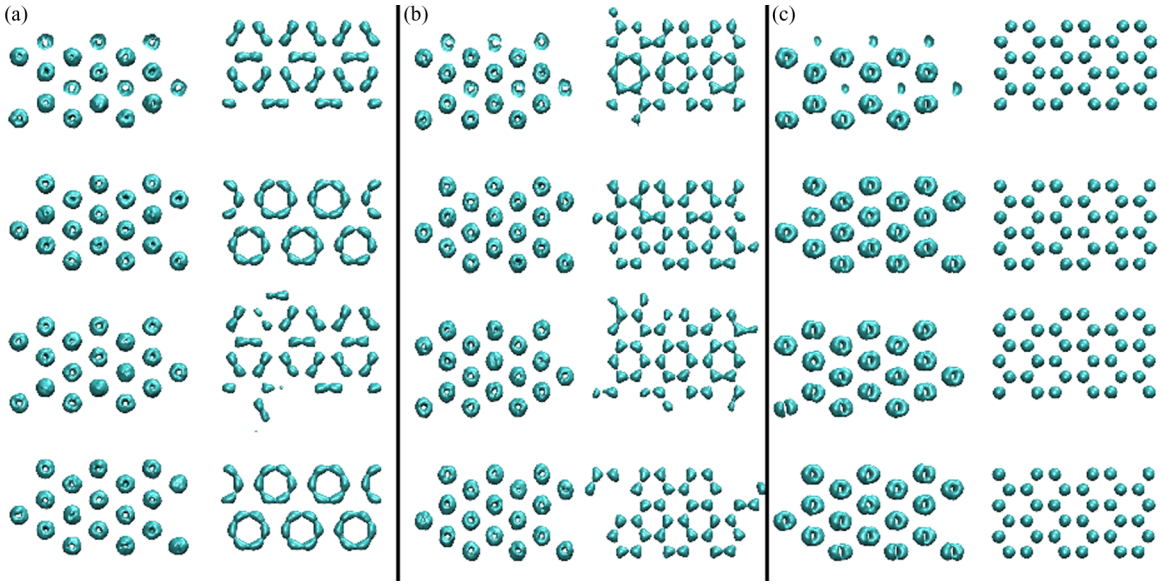

FIG. 2. Isosurfaces of time-averaged probability density for indistinguishable atoms from eight-layer AIMD simulations at different pressures. (a) 250 GPa G′BG″B phase IV. (b) 325 GPa BG′ Phase V. (c) 400 GPa BG atomic molecular.

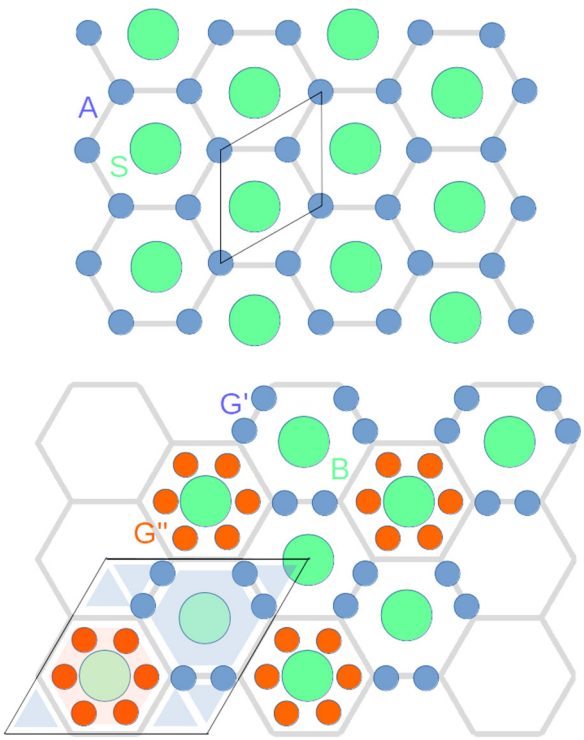

FIG. 3. Idealized geometric stacking patterns for phases IV/IV′/V as deduced from Fig. 2. (Top) Two-layer $P6/mmm$ MgB_2 structure, with S objects on the Mg site and A on the B sites. Thick gray lines showing hexagonal symmetry, thin black line showing primitive cell. Note that the $P6/mmm$ requires only that the S molecule rotates about the z axis, appearing as a donut in Fig. 2. (Bottom) Four-layer BG′BG″ broken symmetry structure with weakly bonded R-type molecules: blue, G′; red, G″; thin black line indicates unit cell of BG′BG″ stacking structure, with G layers at different heights.

pointing in one of three possible directions. The next layer fits efficiently with 2/3 molecules located above the larger interstices and the third above triple-triangular interstice in the center of the figure. The orientation of the molecules is of secondary importance, but it is this that defines the crystal symmetry. All near-neighbor molecules in a layer have different orientations. The $C2/c$-12 structure has a two-layer repeat stacking, with molecules two hcp layers above pointing in the same direction. $C2/c$-24 has a four-layer repeat stacking, while the lowest-energy $P6_122$ structure has a six-layer repeat, cycling through all three possible orientations and giving it the highest symmetry.

It can also be seen that to maintain efficient packing the molecules become asymmetric: the midpoint between nuclei is not precisely at the center of the electron distribution, nor on the hcp lattice site. This causes the molecule to obtain a dipole moment, which is in turn responsible for the strong IR signal, which characterizes phase III.

In all these candidate phases, the rods lie in the plane, so according to the model the c/a ratio should be less than ideal ($\sqrt{8/3}$ for a two-layer repeat). DFT calculation for $P6_122$, for which c/a is uniquely defined, gives a value of 1.549 at 150 GPa dropping to 1.541 at 350 GPa.

Figure 4 shows how the diffusion of phase IV varies with pressure and Fig. 3 gives an insight into the process of the diffusion.

(i) In G″ layers it is possible for two correlated events to occur in the trimers: bond breaking where the definition of molecules changes between two permutations; and trimer rotation through 60°. These two processes are distinct in the classical MD, but equivalent for indistinguishable quantum protons. In either case, all atoms remain within the same hexagonal cell and no diffusion is possible. This rebonding leads to short lifetime of molecular vibration in the G layer, and consequent broadening of the Raman vibron in addition to anharmonic effects [43].

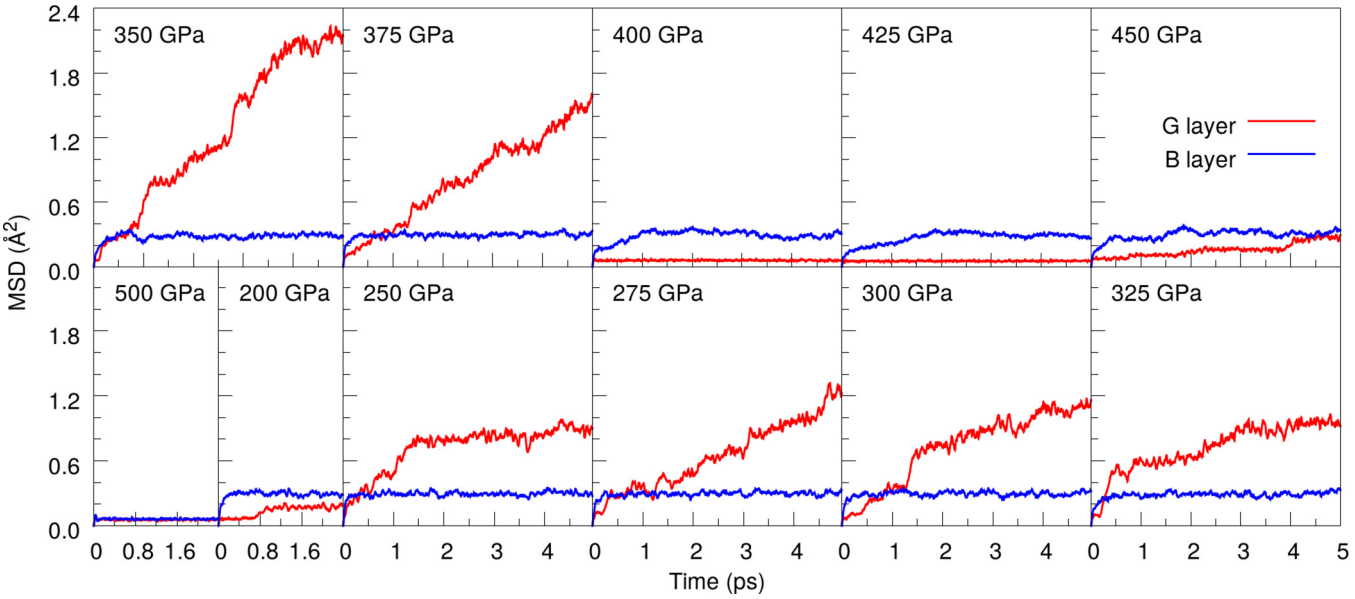

FIG. 4. Mean-squared displacements at 300 K from *ab initio* MD simulations at various pressures. Note the saturation of MSD for rotating molecules in B layers, larger saturated G-layer MSD for rotating trimers in BG″BG′ (250–325 GPa), linearly increasing diffusive MSD for BG′ (350–375 GPa) and no diffusion for atomic G layers (400–450 GPa). This different dynamic behavior distinguishes phases IV, IV′, and V in the MD and in spectroscopy, but it is debatable whether they are thermodynamically distinct phases, so they are all treated equivalently in the model.

(ii) In G^a layers, diffusion cannot occur, except via vacancies.

(iii) In G′ layers molecules are located between two cells. A trimer rotation through 120° leaves the pattern unchanged, however, a sequence of such rotations in neighboring cells can move the molecule through the lattice, giving rise to true diffusion. In the BG″BG′ stacking such rotation is suppressed because the G″ hexagons impose ordering in the G′ layer.

In MD we find that diffusion in the BG′BG″ and BG^a structures, is low, but for the BG′ structure it is significant. This additional diffusion implies increased broadening of spectroscopic lines with increasing pressure—the most notable signature of phase V.

To summarize, we have built a model for the hydrogen phase diagram based around simple concepts and a few descriptive parameters. The model is robust: any sensible choice for the parameters gives a phase diagram including the known phases and unusual behavior of the melting curve. While there is no doubt that a quantitative theoretical description of the phase diagram requires complex quantum treatment of both protons and electrons, it is remarkable that the overall picture can be captured with classical free energies.

In addition to reproducing known phases, the model makes a number of predictions, which can be used to guide analysis of future, more detailed calculations, namely,

(i) The melting point maximum is due to the liquid being a mix of large and small objects.

(ii) The liquid metal-insulator transition has a percolation/localization character.

(iii) Phase III should be thought of as closely packed molecules, somewhat elongated but close to spherical, rather than layers of atoms.

(iv) Isotope effects are generally reported at lower pressure in deuterium compared to hydrogen: this could equivalently

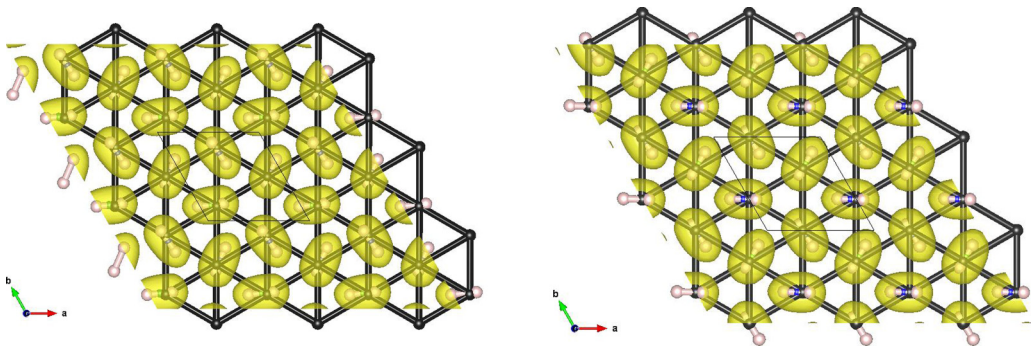

FIG. 5. Electron localization function isosurface (ELF = 0.5) for one plane of phase III candidate structures (a) $C2/c$ [16] and (b) $P6_122$ [21], illustrating the rationale for modeling it in terms of efficient packing of rodlike molecules. Pink spheres correspond to the hydrogen atoms, whereas smaller blue (green) spheres are located at the midpoints of the two types of molecules, with slightly larger (shorter) bond lengths. Black spheres and lines represent the hcp packing, and show that the molecular centers can be regarded as almost close packed.

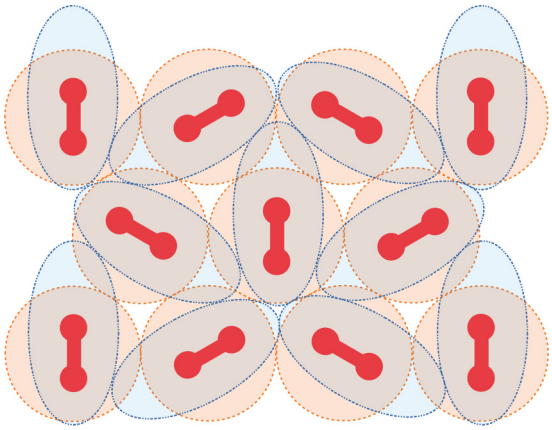

FIG. 6. Geometric stacking patterns for phase III, where conventional layered structure molecules (red dumbbells) are centered on spheres, illustrating the hexagonal close packing interpretation. The dumbbell orientation is common to the proposed $C2c$ or $P6_122$ [21]. The ellipses show how the orientation of R objects gives efficient packing of ellipsoids as a distortion from hcp [35].

be described as shifted to higher temperature, which is our approach. The consequence is that isotope effects are far more pronounced in transitions with shallow Clapeyron slopes.

(v) Efficient packing of ellipsoids in phase III leads to molecular asymmetry, a dipole moment, and explains the strong IR signal.

(vi) The metallic phase VI of our model need not be closely packed, the increased density arises from the atoms being smaller than molecules.

(vii) Phase IV adopts a time-averaged structure, which represents the known most efficient close packing of binary hard spheres. Hence it is stabilized by packing effects as well as entropy.

Note added in proof. Ref [36] has appeared since the completion of our study. It reports two phases named PRE and MH beyond III and V. Within our model both would be represented by the atomic phase VI. Two such phases can be accommodated in the model by allowing for some additional binding energy U_{PRE} and a more efficient packing $c_{\mathrm{PRE}} < c_{\mathrm{MH}}$. The nature of that binding U_{PRE} is not clear, by analogy with other simple metals is might be an electride or a Fermi surface effect.

We thank E. Gregoryanz, A. Hermann, C. Pickard, I. Silvera, B. Monserrat, and M. Martinez-Canales for many useful discussions. We thank Engineering and Physical Science Research Council for computing time (UKCP Grant K01465X) and for the support of a scholarship (I.B.M.). G.J.A. was supported by an European Research Council fellowship "Hecate" and a Royal Society Wolfson fellowship.

[1] R. T. Howie, C. L. Guillaume, T. Scheler, A. F. Goncharov, and E. Gregoryanz, Phys. Rev. Lett. **108**, 125501 (2012).
[2] M. Eremets and I. Troyan, Nature Mater. **10**, 927 (2011).
[3] C.-s. Zha, R. E. Cohen, H.-K. Mao, and R. J. Hemley, Proc. Natl. Acad. Sci. USA **111**, 4792 (2014).
[4] P. Dalladay-Simpson, R. T. Howie, and E. Gregoryanz, Nature (London) **529**, 63 (2016).
[5] M. Eremets, I. Troyan, and A. Drozdov, arXiv:1601.04479.
[6] R. P. Dias, O. Noked, and I. F. Silvera, Phys. Rev. Lett. **116**, 145501 (2016).
[7] N. W. Ashcroft, J. Phys. Condens. Matter **12**, A129 (2000).
[8] E. Babaev, A. Sudbø, and N. Ashcroft, Nature (London) **431**, 666 (2004).
[9] S. A. Bonev, E. Schwegler, T. Ogitsu, and G. Galli, Nature (London) **431**, 669 (2004).
[10] R. T. Howie, P. Dalladay-Simpson, and E. Gregoryanz, Nature Mater. **14**, 495 (2015).
[11] H. Y. Geng, R. Hoffmann, and Q. Wu, Phys. Rev. B **92**, 104103 (2015).
[12] J. Chen, X.-Z. Li, Q. Zhang, M. I. Probert, C. J. Pickard, R. J. Needs, A. Michaelides, and E. Wang, Nature Commun. **4**, 2064 (2013).
[13] J. M. McMahon, M. A. Morales, C. Pierleoni, and D. M. Ceperley, Rev. Mod. Phys. **84**, 1607 (2012).
[14] A. F. Goncharov, R. T. Howie, and E. Gregoryanz, Low Temp. Phys. **39**, 402 (2013).
[15] C. J. Pickard and R. J. Needs, Nature Phys. **3**, 473 (2007).
[16] C. J. Pickard and R. J. Needs, Phys. Status Solidi B **246**, 536 (2009).
[17] C. J. Pickard, M. Martinez-Canales, and R. J. Needs, Phys. Rev. B **85**, 214114 (2012).
[18] H. Y. Geng, H. X. Song, J. Li, and Q. Wu, J. Appl. Phys. **111**, 063510 (2012).
[19] H. Liu, H. Wang, and Y. Ma, J. Phys. Chem. C **116**, 9221 (2012).
[20] V. Labet, R. Hoffmann, and N. Ashcroft, J. Chem. Phys. **136**, 074501 (2012).
[21] B. Monserrat, R. J. Needs, E. Gregoryanz, and C. J. Pickard, Phys. Rev. B **94**, 134101 (2016).
[22] H. Liu, L. Zhu, W. Cui, and Y. Ma, J. Chem. Phys. **137**, 074501 (2012).
[23] I. B. Magdău and G. J. Ackland, Phys. Rev. B **87**, 174110 (2013).
[24] I. B. Magdău and G. J. Ackland, J. Phys.: Conf. Ser. **500**, 032012 (2014).
[25] G. J. Ackland and I. B. Magdău, Cogent Physics **2**, 1049477 (2015).
[26] R. C. Clay III, J. McMinis, J. M. McMahon, C. Pierleoni, D. M. Ceperley, and M. A. Morales, Phys. Rev. B **89**, 184106 (2014).
[27] S. Azadi and W. M. C. Foulkes, Phys. Rev. B **88**, 014115 (2013).
[28] S. Azadi, W. Foulkes, and T. D. Kühne, New J. Phys. **15**, 113005 (2013).
[29] S. Azadi, B. Monserrat, W. M. C. Foulkes, and R. J. Needs, Phys. Rev. Lett. **112**, 165501 (2014).
[30] J. Chen, X. Ren, X.-Z. Li, D. Alfè, and E. Wang, J. Chem. Phys. **141**, 024501 (2014).
[31] J. McMinis, R. C. Clay III, D. Lee, and M. A. Morales, Phys. Rev. Lett. **114**, 105305 (2015).

[32] N. D. Drummond, B. Monserrat, J. H. Lloyd-Williams, P. L. Ríos, C. J. Pickard, and R. J. Needs, Nature Commun. **6**, 7794 (2015).
[33] I. I. Mazin, R. J. Hemley, A. F. Goncharov, M. Hanfland, and H.-K. Mao, Phys. Rev. Lett. **78**, 1066 (1997).
[34] P. Loubeyre, F. Occelli, and R. LeToullec, Nature (London) **416**, 613 (2002).
[35] Y. Akahama, M. Nishimura, H. Kawamura, N. Hirao, Y. Ohishi, and K. Takemura, Phys. Rev. B **82**, 060101 (2010).
[36] R. P. Dias and I. F. Silvera, Science **355**, 715 (2017).
[37] K. A. Johnson and N. Ashcroft, Nature (London) **403**, 632 (2000).
[38] M. A. Morales, C. Pierleoni, E. Schwegler, and D. Ceperley, Proc. Natl. Acad. Sci. USA **107**, 12799 (2010).
[39] H. Kitamura, S. Tsuneyuki, T. Ogitsu, and T. Miyake, Nature (London) **404**, 259 (2000).
[40] M. A. Morales, J. M. McMahon, C. Pierleoni, and D. M. Ceperley, Phys. Rev. Lett. **110**, 065702 (2013).
[41] M. Born and K. Huang, *Dynamical theory of crystal lattices* (Oxford University Press, Oxford, 1954).
[42] G. J. Ackland, J. Phys. Condens. Matter **14**, 2975 (2002).
[43] B. Monserrat, N. D. Drummond, and R. J. Needs, Phys. Rev. B **87**, 144302 (2013).
[44] D. Marx and M. Parrinello, Z. Phys. B **95**, 143 (1994).
[45] See Supplemental Material at http://link.aps.org/supplemental/10.1103/PhysRevB.95.094107 for details of DFT calculations, construction of the reference phase boundaries with uncertainties from previous experimental data and parameter sensitivity analysis for the fitting.
[46] M. A. Morales, J. M. McMahon, C. Pierleoni, and D. M. Ceperley, Phys. Rev. B **87**, 184107 (2013).
[47] M. Knudson, M. Desjarlais, A. Becker, R. Lemke, K. Cochrane, M. Savage, D. Bliss, T. Mattsson, and R. Redmer, Science **348**, 1455 (2015).
[48] G. J. Ackland, Science **348**, 1429 (2015).
[49] G. J. Ackland and I. B. Magdău, Open data http://dx.doi.org/10.7488/ds/364, 2016.
[50] I. B. Magdău, https://www.youtube.com/watch?v=x5WpbRCoHfU, 2015.
[51] R. LeSar and D. Herschbach, J. Phys. Chem. **85**, 3787 (1981).